



Cite this: *Soft Matter*, 2025,
21, 68

Crowding effects on the structure and rheology of ultrasoft PNIPAM–PEGMA copolymer microgels†

Gavino Bassu,^{ab} Jacopo Vialeto,^{ab} José Ruiz-Franco,^{cd} Andrea Scotti,^{de} Judith E. Houston,^f Jitendra Mata,^{gh} Emanuela Zaccarelli^{ij} and Marco Laurati^{ab}                  

We investigate the link between the internal microstructure of poly(*N*-isopropylacrylamide)–poly(ethylene glycol) methyl ether methacrylate (PNIPAM–PEGMA) microgels, their bulk moduli and the rheological response and structural arrangement in dense suspensions. The low degree of crosslinking combined with the increased hydrophilicity induced by the presence of PEGMA results in a diffuse, star-like density profile of the particle and very low values of the bulk modulus in dilute conditions, as determined by small angle neutron scattering (SANS). The ultrasoft nature of the particle is reflected in the changes of the structural arrangement in dense suspensions, which evidence a strong deswelling and a sharp rise of the bulk modulus at moderate packing fractions. At larger packings the single particle morphology and softness saturate, and we observe a structural transition from a dispersion-like to a hydrogel-like behavior. The transition is also reflected in the rheological response in the form of a two-step yielding at large packing fractions, characteristic of systems in which a network structure is present. Our results demonstrate that a knowledge of the internal structure and mechanics of individual microgels is needed to determine and tune the properties of dense suspensions, and optimize their response for applications in biomedicine and as filtration systems.

Received 16th September 2024,
Accepted 22nd November 2024

DOI: 10.1039/d4sm01103a

rsc.li/soft-matter-journal

1 Introduction

Microgels are soft colloidal particles formed by cross-linked polymer networks. The properties of the polymers forming the network make them responsive to stimuli like temperature,¹

pH,^{2,3} light,⁴ among others. This responsiveness is appealing for applications and can be also used to tune their physico-chemical properties to address fundamental physics questions. Thermoresponsive microgels composed of poly(*N*-isopropylacrylamide) (PNIPAM) have been thoroughly studied for several years. They undergo a volume phase transition (VPT) at $T_c \approx 32$ °C^{5,6} from a swollen to a collapsed state, associated with the hydrophilic to hydrophobic transition of PNIPAM.⁷ This results also in a change in particle softness.^{8,9} When following a batch precipitation polymerization route their internal microstructure is characterized by a non-uniform density profile, consisting of a denser core and a more diffuse corona¹⁰ that contains dangling ends.^{11,12} This microstructure can be manipulated through the synthetic process,^{13,14} the degree of crosslinking^{15,16} and the presence of a copolymer,^{17,18} resulting in different degrees of heterogeneity and different amounts and distributions of the crosslinkers within the gel network. These changes in turn determine the mechanical response of single particles and also affect the rheological response of suspensions in the linear and non-linear regimes^{19,20} and the interaction with surfaces and interfaces.²¹ The individual particle softness can be quantified by measuring the elastic modulus of the microgels using atomic force microscopy²² or micropipette aspiration,²³ or the bulk

^a Dipartimento di Chimica “Ugo Schiff”, Università di Firenze, Sesto Fiorentino (FI) 50019, Italy. E-mail: marco.laurati@unifi.it

^b Consorzio per lo Sviluppo dei Sistemi a Grande Interfase (CSGI), via della Lastruccia 3, Sesto Fiorentino (FI) 50019, Italy

^c Department of Condensed Matter Physics, University of Barcelona, 08028 Barcelona, Spain

^d Institute for Complex Systems (UBICS), University of Barcelona, 08028 Barcelona, Spain

^e Division of Physical Chemistry, Lund University, SE-22100 Lund, Sweden

^f European Spallation Source ERIC, Box 176, SE-22100 Lund, Sweden

^g Australian Centre for Neutron Scattering (ACNS), Australian Nuclear Science and Technology Organisation (ANSTO), Lucas Heights, New South Wales 2234, Australia

^h School of Chemistry, University of New South Wales, NSW, Australia

ⁱ Department of Physics, Sapienza University of Rome, Piazzale Aldo Moro 2, 00185 Roma, Italy

^j CNR Institute of Complex Systems, UoS Sapienza, Piazzale Aldo Moro 2, 00185 Roma, Italy

† Electronic supplementary information (ESI) available. See DOI: <https://doi.org/10.1039/d4sm01103a>



modulus by applying osmotic stress combined with dynamic light scattering²⁴ or small angle neutron scattering (SANS) with contrast variation.^{25,26} Application of osmotic stresses is obtained by dispersing the microgels in solutions of non-adсорbing polymers with different concentrations. Measurement of the microgel size as a function of osmotic pressure through SANS, by contrast matching the scattering contribution of the deuterated polymer, allows to determine the bulk modulus.^{25,26} Moreover, SANS is particularly suitable for nanometric microgels due to the accessible range of scattering vectors. The microgel internal microstructure is also closely connected to the phase behavior of the corresponding suspensions.²⁷ In particular, recent studies on PNIPAM microgels showed that when the packing fraction exceeds random-close-packing, the core-corona structure of these particles and the presence of dangling ends give rise to different mechanisms by which the microgels can adapt to overpacking, namely deformation and faceting, interpenetration and isotropic compression.²⁸ These variations in the internal microstructure were also linked to the rheological response.²⁹ However, this study was limited to a degree of crosslinking (5 mol%) of PNIPAM microgels, corresponding to relatively stiff particles with an internal microstructure that can be modeled as a fuzzy sphere. Therefore, the interplay between the internal architecture and the softness of the network in determining the phase behavior and rheological properties of microgels is still largely unexplored.

In this work, we investigate such interplay for the case of copolymer microgels formed by PNIPAM and poly(ethylene glycol) methyl ether methacrylate (PEGMA). Being non-cytotoxic,³⁰ the presence of PEGMA increases the biocompatibility of thermoresponsive PNIPAM microgels in view of biomedical applications.^{31–33} The PEGMA used in this work has no measurable low critical solution temperature (LCST)³⁴ due to its large molecular weight ($M_n = 950 \text{ g mol}^{-1}$) and is thus non-thermoresponsive. Shorter PEGMA alone or in combination with other copolymers can be also used to form microgels, that for smaller M_n can be thermoresponsive with tunable VPT temperature.³⁵ In a recent work, we showed that for low cross-linking degree (1 mol%) PNIPAM–PEGMA copolymer microgels obtained in one-batch synthesis present a very diffuse, star-like polymer density profile and an inhomogeneous collapse, with the VPT transition shifted to higher temperatures compared to pure PNIPAM microgels.¹⁸ Furthermore, the presence of PEGMA modifies the interparticle interactions, in particular above the VPT temperature, and the resulting phase behavior.³⁶ Here, we first link the internal microstructure of PNIPAM–PEGMA microgels to the mechanical properties of the individual particles by measuring the bulk modulus of microgels dispersed in PEG solutions through SANS. We find that the low crosslinking degree and star-like profile result in ultrasoft colloids. We then explore the effects of the internal microstructure and associated softness on the phase behavior of dense packings, analyzing scattering intensities obtained by small angle X-rays scattering (SAXS). We find that particles deswell significantly at moderate packing fractions, even smaller than what previously observed for pure PNIPAM microgels,³⁷ and we

link this unusual response to the single particle mechanical properties. When the particles become mechanically harder following deswelling,²⁵ a saturation of the structural changes is instead observed and the structural organization of the system resembles that of a hydrogel network. The structural changes have a signature in the non-linear rheological response of the system, with the appearance of a second yielding process when the structural saturation occurs. Our findings provide evidence of the close connection between internal architecture, individual particle softness and rheological response of dense microgel suspensions, showing how this could be manipulated in view of applications.

2 Materials and methods

2.1 Experimental system

2.1.1 Microgel synthesis. PNIPAM–PEGMA copolymer microgels were prepared following a “one pot” soapless emulsion polymerization synthesis,³⁸ using ethylene glycol dimethacrylate (EGDMA) as crosslinker and ammonium persulfate (APS) ($M_n = 228.18 \text{ g mol}^{-1}$) as initiator. All reagents were purchased from Merck. NIPAM ($M_n = 113.16 \text{ g mol}^{-1}$) was purified by recrystallization in 40/60 v/v toluene/hexane. EGDMA, APS and PEGMA ($M_n = 950 \text{ g mol}^{-1}$) were used as purchased. The synthesis was performed in a 1 L three-neck flask placed in a heating oil bath. The weight fraction of the two polymers in the reaction was equal to 30% PEGMA and 70% PNIPAM. Initially, 3.5 g of PNIPAM and 1.5 g of PEGMA were dissolved in 438 ml of water and mixed with the EGDMA crosslinker (1 mol% vs. PNIPAM). The so-obtained solution was bubbled with nitrogen for 1 hour to remove any dissolved oxygen while being stirred at 350 rpm at room temperature. The reaction mixture was then heated at 85 °C while stirring at 350 rpm and equilibrated for 30 minutes. APS (2 wt% vs. PNIPAM) previously dissolved in 12 ml of water was bubbled with nitrogen for 30 minutes and then added drop-wise to the reaction mixture to initiate the polymerization. After 45 minutes of reaction, the solution was placed in an ice bath to stop the polymerization process. The polymeric dispersion was purified through dialysis, using a membrane with a molecular weight cut-off of 12–14 kDa, in distilled water for 7 days. The microgels were then centrifuged at 23 000 rcf for 20 minutes in order to remove any residual impurity and were subsequently recovered by freeze-drying. ¹H-NMR characterization showed that the effective incorporation of PEGMA corresponded to a weight proportion of 66% PNIPAM and 34% PEGMA.³⁶ The hydrodynamic radius of the microgels was determined by dynamic light scattering, $R_H \approx 144 \text{ nm}$ in water at low temperature $T = 20 \text{ }^\circ\text{C}$ and decreases to $R_H \approx 78 \text{ nm}$ at high $T = 50 \text{ }^\circ\text{C}$, with the VPT occurring at $T_c \approx 36 \text{ }^\circ\text{C}$ (see Fig. S1 of the ESI† for the entire R_H vs. T dependence). The value of the VPT temperature T_c , also later called VPTT, is higher than that of pure PNIPAM microgels in water ($T_c \approx 32 \text{ }^\circ\text{C}$).

2.1.2 Preparation of dispersions. For SAXS measurements dispersions with w/w concentrations $c = 7, 9, 14, 18, 20$ and 22% were prepared by redispersing the dry microgel powder in



deionized water. After water addition, samples were mixed at 30 °C first in an orbital shaker and later using a magnetic stirrer until complete homogenization. Samples were filled into 1.5 mm thick borosilicate glass capillaries for measurement. The effective volume fractions (ϕ_{eff}) of the samples at $T = 20$ °C were defined, following previous work,^{39,40} as $\phi_{\text{eff}} = c[R_{\text{H}}(T = 20\text{ }^{\circ}\text{C})/R_{\text{H}}(T = 50\text{ }^{\circ}\text{C})]^3$. The values of ϕ_{eff} calculated with this definition closely match ϕ values from simulations for moderate concentrations.³⁶ Additionally, different regimes of the rheological response of these suspensions are observed at ϕ_{eff} values comparable to those of PNIPAM microgel suspensions with comparable crosslinking degree.⁴⁰ The effective volume fractions for samples at $T = 20$ °C are $\phi_{\text{eff}} = 0.48, 0.61, 0.95, 1.22, 1.30, 1.41, 1.49$. For SANS measurements, mixtures of microgels and partially deuterated PEG (d_{85%}PEG, $M_w = 260$ kDa, 85% deuteration) in D₂O were prepared by diluting stock solutions (in turn prepared in D₂O) at the required concentration of d_{85%}PEG, fixing the content of microgels at 0.1 w/w%. The obtained samples were then mixed at room temperature in an orbital shaker overnight.

2.2 Small-angle neutron and X-ray scattering (SANS/SAXS)

2.2.1 Measurements. SANS measurements were performed at Quokka (ANSTO, Sydney, Australia)⁴¹ using the following configuration: (i) 1.35 m sample-to-detector distance (SDD) and incident wavelength $\lambda = 5.5$ Å, (ii) 12 m SDD and $\lambda = 5.5$ Å, and (iii) 20 m SDD and $\lambda = 8.1$ Å using lens optics. The combination of the three configurations gives a wave vector range $0.0007\text{ }{\text{\AA}}^{-1} < Q < 0.66\text{ }{\text{\AA}}^{-1}$. A Quokka macro in Igor Pro software (Wavemetrics, Lake Oswego, Oregon, USA), originally written by Kline,⁴² was used for data reduction. The samples were measured at $T = 20$ °C in quartz cells with a path length of 2 mm (Hellma GmbH & Co., Mullheim, Germany).

SAXS measurements for $\phi_{\text{eff}} = 0.48, 0.61$ and 0.95 were performed on a Xeuss 3.0 HR (Xenocs, Grenoble, France) using a 1028×1062 pixels (pixel size $75 \times 75\text{ }\mu\text{m}^2$) EIGER2R 1 M hybrid pixel photon counting detector (Dectris Ltd, Baden, Switzerland). The wavelength of the X-ray beam was $\lambda = 1.542$ Å. The sample chamber was maintained at atmospheric pressure. A sample-to-detector distance of 1800 mm was used to access a Q -range of 0.004 to $0.14\text{ }{\text{\AA}}^{-1}$. Microgel suspensions were contained in 1.5 mm thick borosilicate glass capillaries sealed with glue to avoid evaporation. Absolute scattering intensities in cm^{-1} were obtained by using glassy carbon as a secondary standard. The 1D azimuthally averaged scattering patterns were reduced by subtracting the scattering intensity from empty holder plus water. Data reduction, normalization, and merging was performed in XSACT (X-ray scattering analysis and calculation tool, Xenocs, France). Additional measurements for $\phi_{\text{eff}} = 1.22, 1.30, 1.41$ and 1.49 were performed at the CoSAXS beamline at the 3 GeV ring of the MAX-IV Laboratory (Lund, Sweden). The Q -range of interest in between 7×10^{-4} and $7 \times 10^{-2}\text{ }{\text{\AA}}^{-1}$ was covered on CoSAXS using a sample-to-detector distance of 14.2 m with X-ray beam energy $E = 12.4$ keV. The instrument is equipped with an Eiger2 4 M SAXS detector with pixel size of $75 \times 75\text{ }\mu\text{m}^2$. A python-based code was used to convert the 2D images to 1D profiles.

2.2.2 Data analysis: determination of the bulk modulus of the microgels. For the determination of the bulk modulus of the microgels we followed the approach recently introduced by Houston and coworkers.²⁵ The first step of this approach is the determination of the microgel radius as a function of d_{85%}PEG concentration. Since the d_{85%}PEG is partially deuterated such that its scattering length density is contrast matched in pure D₂O, the SANS scattered intensities measured for microgel-d_{85%}PEG mixtures can be expressed as:⁴³

$$I(Q) = \phi V(\Delta\rho)^2 P(Q)S(Q) + \text{bkg} \quad (1)$$

where ϕ is the volume fraction of microgels, V the microgel volume, $\Delta\rho = \rho_1 - \rho_2$ the scattering length density difference between the microgels (ρ_1) and D₂O (ρ_2), $P(Q)$ the particle form factor. Due to the low microgel concentration, structure factor contributions are negligible and therefore $S(Q) = 1$. The term bkg indicates background. In previous work¹⁸ we have shown that the particle form factor of these microgels can be modeled using the star polymer form factor function of Dozier and coworkers,^{44,45} that is composed of two terms:

$$P(Q) = A_1 \exp\left[-\frac{1}{3}Q^2 R_g^2\right] + A_2 \frac{\sin(\mu \tan^{-1}(Q\xi))}{Q\xi(1 + Q^2\xi^2)^{\mu/2}} \quad (2)$$

The first term is used to model the Guinier regime and provides the particle radius of gyration R_g . The second term describes the blob scattering of the star arms and allows the blob size ξ to be determined. This represents the characteristic length scale at which the granular polymer structure becomes relevant. The exponent μ is defined as $\mu = 1/\nu - 1$, being ν the Flory exponent. The amplitudes A_1 and A_2 weight the contributions of the two terms.

Using R_g we calculate the microgel volume v and we correlate it with the known osmotic pressure π of the d_{85%}PEG solutions. The concentrations of d_{85%}PEG are converted in π using the empirical law from Houston *et al.*,²⁵ measured using a membrane osmometer, and are chosen in order to cover a range between 0 and ~ 100 kPa. The bulk modulus K is then determined from the slope of the π vs. v curves: $K = -v\text{d}\pi/\text{d}v$.

2.2.3 Data analysis: modeling of concentrated microgel suspensions. Concentrated suspensions were modeled using eqn (1), in which this time the $S(Q)$ contribution was included. For modeling $P(Q)$ we used again eqn (2), in which now R_g and ξ are dependent on ϕ_{eff} .

Following previous studies,³⁶ $S(Q)$ was obtained from Langevin dynamics simulations of $N = 2000$ particles with mass m and polydispersity 0.25. These particles interact by a Hertzian potential, which is expressed as

$$V(r) = U(1 - r/\sigma)^{5/2}\theta(\sigma - r), \quad (3)$$

where U represents the Hertzian strength linked to the particle elasticity and σ represents the particle diameter. The Heaviside step function θ ensures the interaction vanishes at distances $r > \sigma$. According to previous analyses,³⁶ the swollen case is well described by fixing $U = 674.1k_{\text{B}}T$ at small ϕ_{eff} , where k_{B} is the Boltzmann constant. The structure factors obtained in this way

were interpolated on the Q values of the experimental data. The packing fraction of the $S(Q)$ that best fits the experimental data provides an estimate of the true packing fraction of the system.

For $\phi_{\text{eff}} > 1$ an additional term was included in eqn (1) to describe the excess scattering at low Q values. This regime was described with the Debye–Bueche model⁴⁶ for solid-like heterogeneities of average size a :

$$I_{\text{DB}}(Q) = \frac{I_{\text{DB}}(0)}{(1 + a^2 Q^2)^2} \quad (4)$$

in which $I_{\text{DB}}(0)$ is the excess scattering at $q = 0$, which is again related to the contrast and the volume fraction of the heterogeneities. This term models the presence of microgel aggregates of average size a at high packing fractions.

2.3 Rheology

All measurements were performed on a DHR-3 (TA Instruments) stress-controlled rheometer. The eventual presence of wall slip effects was preliminary tested through the measurement of the dependence of the sample viscosity on the gap size obtained with a 20 mm smooth plate-plate geometry. For samples with $\phi_{\text{eff}} > 0.48$ no indications of slip were found and a cone-plate geometry with a 40 mm diameter and a cone angle of 0.5081° was used for all tests. For $\phi_{\text{eff}} = 0.48$ we found indications of wall slip and therefore a crosshatched plate-plate geometry with diameter 40 mm was used instead. Temperature was controlled through a Peltier lower plate and it was fixed to 20°C . To avoid evaporation, a solvent trap was used.

In order to minimize the effects of sample history, a rejuvenation protocol was applied before each measurement. First, an oscillatory dynamic time sweep with a large strain amplitude ($100\% < \gamma_0 < 700\%$, depending on sample) was applied for 180 s. This was followed by a dynamic time sweep with a low strain amplitude ($0.05\% < \gamma_0 < 0.2\%$, depending on sample) that was stopped when a steady state in the viscoelastic moduli was reached. We found that 180 s were sufficient to reach the steady state for all samples. The frequency used for the two time sweeps was $\omega = 10 \text{ rad s}^{-1}$.

3 Results and discussion

3.1 Form factor and bulk modulus

The particle form factor of the microgels was determined from the SANS measurement of a dilute suspension and is shown as the bottom curve in Fig. 1. The very smooth Q -dependence of the scattered intensity $I(Q)$, with no clear indication of a minimum, indicates a very diffuse density profile together with significant polydispersity. $I(Q)$ was modeled according to eqn (1) and the star polymer form factor model of eqn (2) (Fig. 1). The fitting leads to a value for the radius of gyration $R_g = 900 \pm 20 \text{ \AA}$ and a blob size $\xi = 300 \pm 10 \text{ \AA}$, with $\nu = 0.66$ and a polydispersity of about 25%, in good agreement with previous findings.¹⁸ The other curves in Fig. 1 corresponds to the scattered intensities measured for microgel-d_{85%}PEG mixtures used to estimate the bulk modulus of the microgels.

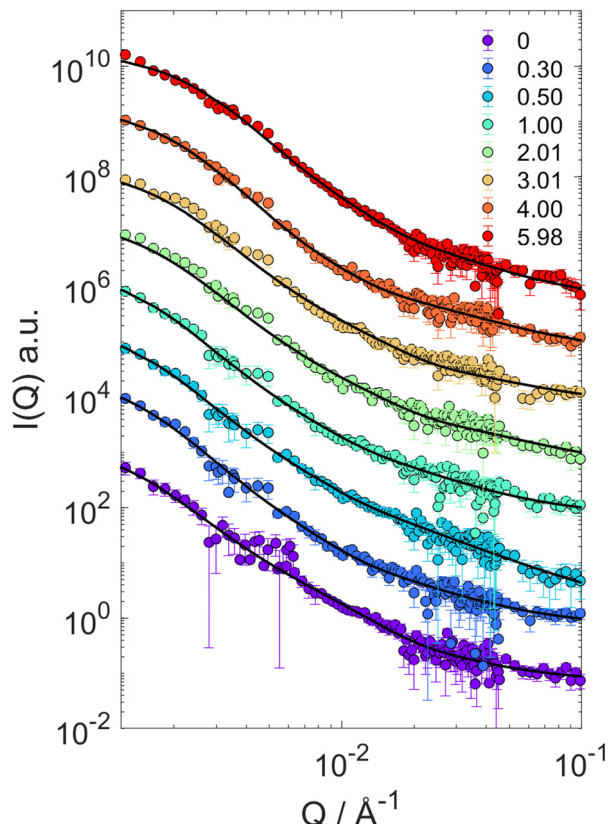


Fig. 1 SANS scattering intensities $I(Q)$ for mixtures of PNIPAM–PEGMA microgels and d_{85%}PEG with increasing d_{85%}PEG concentration (as indicated). Lines represent fits of the microgel form factor using the star polymer model of eqn (2).

The d_{85%}PEG concentration increases from bottom to top and varies between 0.30 and 5.98 wt% (top curve). It can be observed that with increasing d_{85%}PEG amount the Guinier regime of the curves progressively shifts to larger Q values, as an effect of microgel deswelling induced by the increasing osmotic pressure produced by the d_{85%}PEG solution. The curves were modeled also in this case using eqn (1) and (2) and the corresponding fits are shown in Fig. 1.

The progressive decrease of the value of R_g obtained from fits as a function of d_{85%}PEG concentration is shown in Fig. S2 of the ESI.[†] These values were used to determine the particle volume $\nu = 4\pi R_H^3/3$, that was normalized to the value in the absence of d_{85%}PEG ($\nu_0 = 4\pi(R_H^0)^3/3$). Note that in the calculation we ignored the proportionality factor between R_H and R_g since the modulus only depends on the slope of the π vs. ν/ν_0 curves. Fig. 2a shows the osmotic pressure as a function of ν/ν_0 , the dashed lines are the fits used to determine the bulk modulus K of the microgel in different compression regimes (more details in the Materials and methods section). As it can be seen in Fig. 2b, the value of K in the low compression regime is about $3.7 \pm 1.6 \text{ kPa}$, which confirms previous estimates³⁶ and is comparable to that of ultra-low crosslinked microgels.²⁵ As expected and similar to the case of the ultra-low crosslinked microgels, with increasing osmotic pressure and induced deswelling (smaller R_g/R_g^0), K increases, reaching a value about 2



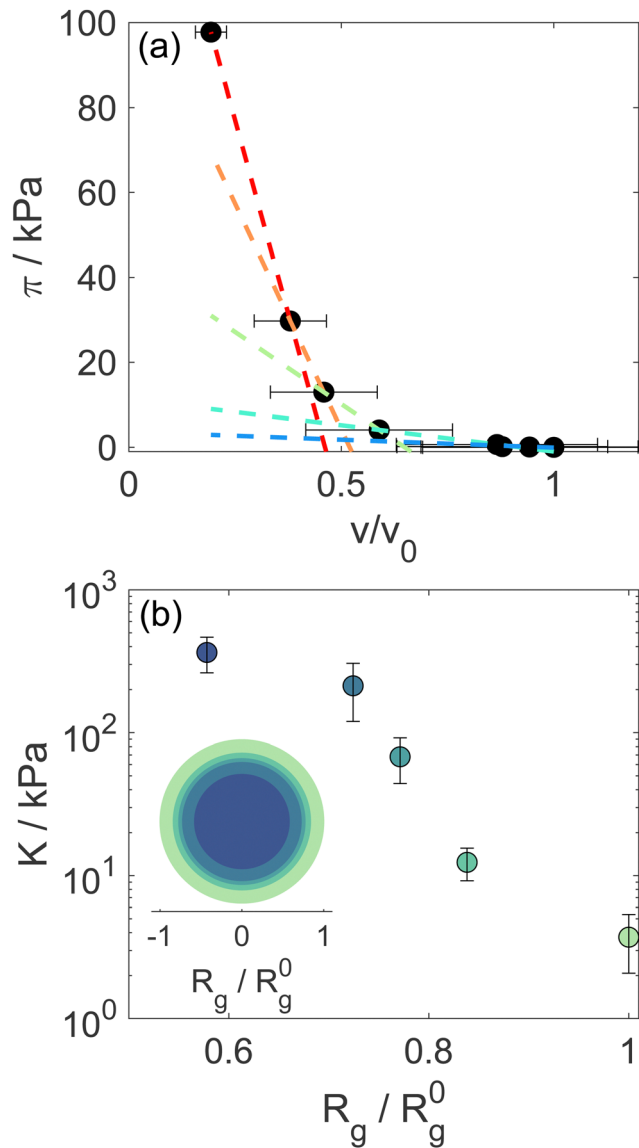


Fig. 2 (a) Osmotic pressure as a function of relative volume variation. Lines are fits used to extract the bulk modulus K of the sample upon increasing particle compression. (b) Microgel's bulk modulus as a function of relative particle size, measured as R_g/R_g^0 , where R_g^0 is the particle radius in the absence of d₈₅-PEG. The inset shows a map of the bulk modulus at different particle compression.

orders of magnitude larger for the highest applied osmotic pressure ($R_g/R_g^0 \approx 0.58$). Interestingly, while the bulk modulus shows the mentioned similarities with ultra-low crosslinked microgels, the deswelling induced by temperature presents differences. Indeed the swelling ratio in response to temperature changes of our star-like microgels is relatively small, $S_D = R_H(T=20\text{ }^\circ\text{C})/R_H(T=50\text{ }^\circ\text{C}) = 1.77 \pm 0.05$ (Fig. S1, ESI†), *i.e.* much lower than that of ultra-low crosslinked microgels, for which $S_D \approx 3.2$,²⁵ and rather comparable to that of regular microgels synthesized with 5 mol% *N,N'*-methylenebis(acrylamide) (BIS) cross-linker ($S_D \approx 1.8$).⁹ We should consider, however, that the presence of non-thermoreponsive PEGMA within the PNIPAM network hinders the temperature-induced collapse of the

microgel, as demonstrated in previous work¹⁸ (while PEGMA on the surface does not affect the collapse¹⁹), in comparison to ultralow crosslinked microgels or PNIPAM microgels with similar star-like architecture having comparable initial value of the modulus. It is interesting to note that the swelling ratio estimated from the reduction of R_g at the largest measured osmotic pressure seems comparable to that of temperature-induced deswelling. However, the microgels could continue shrinking at higher applied osmotic pressures that could not be achieved in our experiments. Thus a conclusive comparison between temperature-induced and compression-induced deswelling cannot be provided in this work. The coexistence of a low modulus with a moderate swelling ratio indicates once more that the relation between these quantities might be complex, since the crosslinking degree, the internal architecture and the responsiveness of the components of a microgel might play a different role in determining them, as already shown by the case of microgels with a solvent-filled cavity in their center.⁴⁷

3.2 Structural arrangement for increasing packing fraction

In previous work³⁶ we characterized the structure and interactions of similar suspensions from the relatively dilute case ($\phi_{\text{eff}} = 0.06$) to intermediate concentrations ($\phi_{\text{eff}} = 0.34$), still well below random close packing. We found that even if the explored packing fractions were moderate, and therefore the pressure exerted by neighbors on a single particle should not be large enough to induce particle shrinking, the size of the particles showed a pronounced reduction with increasing ϕ_{eff} , indicating strong deswelling. As reported in the literature particles synthesized with ionic initiator are slightly charged and surrounded by counter-ion clouds.⁴⁸ Once the particle concentration increases these counter-ion clouds percolate the available volume outside the microgels. This induces an unbalance in the osmotic pressure inside and outside the particles leading to deswelling when it becomes comparable or larger than the bulk modulus of the particles.³⁷ As shown in the previous section, we were now able to determine the bulk modulus of the particles that is comparable to the increase in osmotic pressure reported in the literature,³⁷ confirming their very pronounced softness, therefore supporting that charge effects can become relevant at relatively moderate packing fractions due to the suspension osmotic pressure. To address how this influences the structural evolution also at larger ϕ_{eff} , where contacts are present and provide an additional contribution to the deformation, interpenetration and deswelling of the particles, we extended our study to cover the interval $0.48 \leq \phi_{\text{eff}} \leq 1.49$.

For $\phi_{\text{eff}} < 1$ the SAXS scattering curves in Fig. 3a show clearly the presence of a structure factor peak. Furthermore, with increasing ϕ_{eff} the curves progressively shift to larger Q values. Increasing ϕ_{eff} from 0.48 to 0.61 the shift involves the entire curve, while further increasing ϕ_{eff} to 0.95 the large Q -value part ($Q > 0.015 \text{ \AA}^{-1}$), where the decay of the form factor is observed, only moves slightly. This indicates that structural changes are significant when increasing effective packing fraction from $\phi_{\text{eff}} = 0.48$ to $\phi_{\text{eff}} = 0.61$, while they are more moderate up to $\phi_{\text{eff}} = 0.95$. For the intermediate Q -value



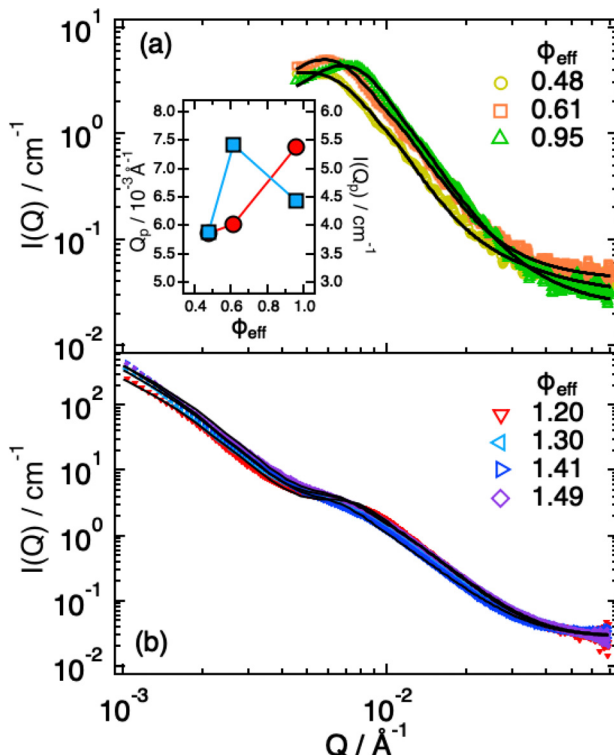


Fig. 3 SAXS intensities $I(Q)$ for $\phi_{\text{eff}} < 1.0$ (a) and $\phi_{\text{eff}} > 1.0$ (b). Lines are fits according to eqn (1), in (b) with the addition of the term from eqn (4). Inset: Dependence of the position (red circles) and height (blue squares) of the $I(Q)$ peak as a function of ϕ_{eff} .

part ($0.004 \text{\AA}^{-1} \leq Q \leq 0.01 \text{\AA}^{-1}$), where the structure factor peak is observed, the shift of the position of the $I(Q)$ ($S(Q)$) peak (Q_p) to larger values (Fig. 3a, inset) means a reduction of the average inter-particle distance. It is interesting to note that, in addition, the $I(Q_p)$ peak first increases in height from $\phi_{\text{eff}} = 0.48$ to $\phi_{\text{eff}} = 0.61$, while it decreases for $\phi_{\text{eff}} = 0.95$ (Fig. 3a, inset), in agreement with what previously observed in simulations³⁶ and explained as a combined effect of the large polydispersity of our system and hertzian interactions.

Modeling of the scattering curves using eqn (1) and (2) and simulated structure factors (lines in Fig. 3a) leads to the determination of the radius of gyration and blob size for the curves in Fig. 3a. The results are reported in Fig. 4a, together with those obtained for larger ϕ_{eff} (that will be discussed later). In all cases a polydispersity $p \approx 0.25$ was obtained from the fits, in agreement with the one used for calculating $S(Q)$ in simulations. As anticipated from the qualitative analysis of the scattering curves, R_g and ξ (inset of Fig. 4a) decrease slightly when increasing ϕ_{eff} . Note that the value of R_g for $\phi_{\text{eff}} = 0.48$ is about a factor 3 smaller than its corresponding value in dilute conditions,³⁶ R_g^0 , indicating a very pronounced particle deswelling/compression. Note also that the values of R_g measured for these packing fractions are almost half of the R_g value measured for the largest osmotic pressure reported in Fig. 2, for which $R_g/R_g^0 \approx 0.58$. A comparable value of $R_g/R_g^0 \approx 0.58$ was obtained for $\phi_{\text{eff}} = 0.24$ in previous work.³⁶ Since the bulk modulus of the particles shows a sharp increase when the

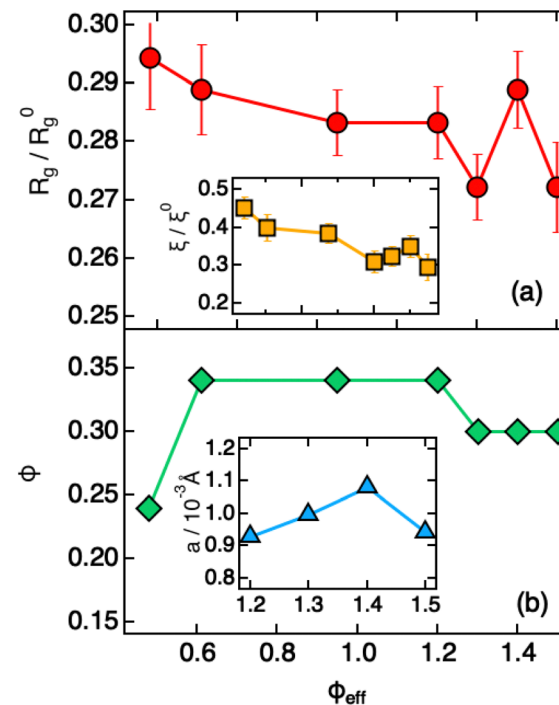


Fig. 4 Parameters extracted from fitting SAXS intensities of Fig. 3 using eqn (1), (2) and (4), plotted as a function of ϕ_{eff} . (a) Reduced radius of gyration R_g/R_g^0 and (inset, same x-axis as the main plot) reduced blob size ξ/ξ_0 . R_g^0 and ξ_0 are the values measured in dilute conditions. (b) Estimated volume fraction (ϕ) and (inset, x-axis values corresponding to ϕ_{eff}) heterogeneity size a .

particle size decreases from 1 to 0.58 as an effect of the increase in osmotic pressure, reaching a value of 364 ± 102 kPa, it is reasonable to assume that for a crowding induced deswelling corresponding to $R_g/R_g^0 \approx 0.31$ at $\phi_{\text{eff}} = 0.48$ the bulk modulus of the particles is $K \gtrsim 350$ kPa: the particles are already very stiff, and the size reduction should become very moderate, as indeed observed in our data, where R_g/R_g^0 decreases to $R_g/R_g^0 \approx 0.26$ for almost double packing fraction, $\phi_{\text{eff}} = 0.95$. Fig. S3 of the ESI† shows R_g/R_g^0 vs. ϕ_{eff} including former data for $0.05 \leq \phi_{\text{eff}} \leq 0.36$, better evidencing the slowdown of the size reduction already at intermediate packing fractions. These results suggest that the structural evolution of single particles in increasingly crowded suspensions can be semi-quantitatively linked to the corresponding evolution of the bulk modulus.

A qualitative change in the scattering curves is observed for $\phi_{\text{eff}} \geq 1.20$ (Fig. 3b): the structure factor peak at intermediate Q values is no longer discernible and for $Q > 2 \times 10^{-2} \text{\AA}^{-1}$ the curves, including the one for $\phi_{\text{eff}} = 0.95$ (not shown), are closely comparable and only slightly shifted toward larger Q values with increasing packing fraction, as expected since polymer chain scattering is observed in this Q range. This suggests that no further morphological variation of the single particles is observed with increasing ϕ_{eff} in this regime. A low Q scattering is observed for all samples, indicating the presence of structural heterogeneities. Modeling of the data with eqn (1) and (2) and with in addition the term in eqn (4) to describe heterogeneities leads to values of R_g and ξ that are closely comparable

to those obtained for $\phi_{\text{eff}} = 0.95$ (Fig. 4a). This confirms that no significant structural variation occurs for $\phi_{\text{eff}} \geq 0.95$, in agreement with the strongly compressed and stiff morphology of the particles. The values of the packing fraction ϕ obtained from the fits are closely comparable for $\phi_{\text{eff}} \geq 0.61$, suggesting a saturation of the local packing of the particles, which coincided with the saturation of deswelling. The size of heterogeneities a for $\phi_{\text{eff}} \geq 1.20$ increases from 910 ± 40 to 1080 ± 50 Å up to $\phi_{\text{eff}} = 1.41$, and decreases again to 900 ± 30 Å for the largest effective packing fraction here investigated. These values correspond to 1.5 to 2 particle diameters, *i.e.* relatively small scale heterogeneities. The small variations of the structural organization of the system for $\phi_{\text{eff}} > 0.61$ suggest the formation of a state that resembles a macroscopic hydrogel at these packing fractions. Indeed the data for $\phi_{\text{eff}} \geq 1.20$ resemble those measured for such systems and can be also modeled in these terms, as shown in Section SIV and Fig. S4 of the ESI.† The structural changes with increasing ϕ_{eff} discussed in this section, namely the strong deswelling at intermediate packing fractions and the formation of a dense, hydrogel-like suspension for $\phi_{\text{eff}} > 0.61$, are sketched in Fig. 5b–e.

3.3 Rheology: signatures of network yielding

We explored possible signatures of the structural transition occurring for $\phi_{\text{eff}} > 0.61$, and sketched in Fig. 5d and e in the rheological response of the system. It has been shown that the non-linear rheological response is especially sensitive to the structural arrangements and interactions of particles in dense suspensions.^{49–52} Fig. 5 shows the results of amplitude sweeps at oscillation frequency $\omega = 1 \text{ rad s}^{-1}$ measured for $\phi_{\text{eff}} = 0.61$, 0.95 and 1.41. The data are reported as elastic stress $G' \gamma_0$ vs. γ_0 (strain amplitude): in this representation the yielding points are clearly evidenced as inflections or maxima.^{49,53} The sample with $\phi_{\text{eff}} = 0.61$ shows initially a linear increase, corresponding to the linear viscoelastic regime, followed by an inflection for $\gamma_0 \approx 80\%$ and then tends to a plateau, indicating the transition to a fluid-like response after yielding, in agreement with findings on colloidal glasses and gels.^{49,54,55} With the increasing of ϕ_{eff} to 0.95 the first inflection is still visible but in addition a second one appears at larger strains, $\gamma_0 \approx 1000\%$. Further increasing ϕ_{eff} to 1.41 the second inflection becomes a pronounced maximum that is observed at approximately the same strain amplitude as for $\phi_{\text{eff}} = 0.95$. In agreement with previous findings on soft, hairy particles,⁴⁰ we interpret the first inflection as the initial restructuring of the sample at the level of nearest neighbors, *i.e.* the breaking of entropic cages.^{54,56} For $\phi_{\text{eff}} = 0.61$ the restructuring of the local order of the colloidal suspension, corresponding to the coordination represented by the structure factor peak, is sufficient to induce complete yielding and the onset of flow. On the other hand, for $\phi_{\text{eff}} \geq 0.95$ the additional network structure formation and the presence of heterogeneities and entanglements with significantly long lifetime does not allow the system to flow. Larger strain amplitudes are necessary to disentangle interpenetrated and compressed coronas of local clusters before this becomes possible. It is interesting to note that even for $\phi_{\text{eff}} \geq 0.95$ the first inflection is present, indicating

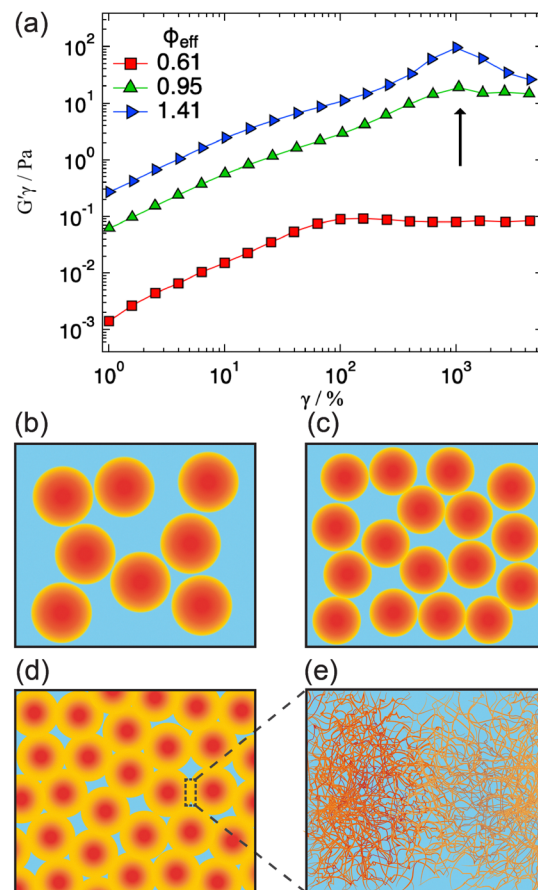


Fig. 5 (a) Elastic stress vs. strain amplitude curves measured in amplitude sweeps performed at an oscillation frequency $\omega = 1 \text{ rad s}^{-1}$ and for different effective volume fractions ϕ_{eff} (as indicated). The arrow indicates the second yield strain associated with temporary polymer entanglements. (b)–(e) Sketch of the microgel packing upon increasing ϕ , indicating deswelling at intermediate ϕ (c), and the transition to a gel-like structure characterized by the formation of a macro network with interpenetration among compressed particles (d) and (e).

that, despite the transition to a gel-like structure, individual particles are still present and can displace with respect to each other under shear. Furthermore, the second yielding occurs at comparable strain amplitudes for $\phi_{\text{eff}} = 0.95$ and 1.41, which seems to be consistent with the fact that the R_g and the characteristic size of the heterogeneities are almost independent of ϕ_{eff} in the gel-like state.

4 Conclusions

We investigated the link between the internal microstructure, the single particle mechanics and the structural arrangement and rheological response of dense suspensions of PNIPAM–PEGMA microgels. The smooth and diffuse star-like density profile of the microgels determined by SANS results in a very low bulk modulus in dilute suspensions, that is comparable to that of ultra-low crosslinked microgels. The large softness of the particles leads to a pronounced reduction of the particle size even at intermediate effective packing fractions. This reduction

slows down above $\phi_{\text{eff}} = 0.48$ and stops for $\phi_{\text{eff}} \geq 0.95$. The slowdown can be linked to the strong rise of the bulk modulus with increasing osmotic pressure. Correspondingly, the structure factor peak that was increasing in height and shifting to larger Q values up to $\phi_{\text{eff}} = 0.61$, indicative of the reduced interparticle distance, starts to decrease until becoming indistinguishable for $\phi_{\text{eff}} > 1$. In this region the scattering curves present a similar shape independent of ϕ_{eff} , that can be described alternatively with a polymer gel network model. This is attributed to the interpenetration of increasingly collapsed coronae that form relatively long-lived entanglements and thus an extended polymer network of connected microgels. This scenario is further supported by the non-linear rheological response of samples with $\phi_{\text{eff}} \geq 1$, in which relaxation of the temporary entanglements leads to a yielding point at large strain amplitudes that, as the gel structure, is almost independent of ϕ_{eff} . A yielding point associated with restructuring of entropic cages is however still present. Our results thus indicate that for ultrasoft microgels with a diffuse density profile and dangling ends, the properties of dense suspensions with $\phi_{\text{eff}} \geq 1$ are strongly influenced by the formation of entanglements between chains and of an extended polymer network. These findings have important implications for applications in which dense suspensions of soft particles are involved, like 3D printing of artificial tissue and the fabrication of anti-fouling surfaces.

Data availability

Data for this article, including raw SANS, SAXS and Rheology data are available at Zenodo at DOI: <https://doi.org/10.5281/zenodo.1376950>.

Conflicts of interest

There are no conflicts to declare.

Acknowledgements

This manuscript is dedicated to Prof. Stefan U. Egelhaaf, an outstanding scientist, wonderful person and true friend. M. L. and E. Z. acknowledge financial support by the Italian Ministry of University and Research (MUR) under the National Recovery and Resilience Plan (NRRP), Mission 4, Component 2, Investment 1.1, Call for tender No. 104 published on 2.2.2022 by the Italian Ministry of University and Research (MUR), funded by the European Union – NextGenerationEU – Project Co-MGELS, contract No. 2022PAYLXW. AS acknowledges financial support from the Knut and Alice Wallenberg Foundation (Wallenberg Academy Fellows). We acknowledge MAX IV Laboratory for time at the CoSAXS beamline under Proposals 20231840 and 20231866, and ANSTO for the time at the Quokka beamline under Proposal P16948. We thank Jürgen Allgaier and Lisa Fruhner for the synthesis of d_{85%}PEG. J. V. acknowledges funding from Ministero dell'Università e della Ricerca (D.D. 247 published on 19.08.2022, grant No. MSCA_0000004),

funded by European Union – NextGenerationEU – PNRR, Mission 4, Componente 2, Investimento 1.2.

Notes and references

- 1 B. Sierra-Martin, J. J. Lietor-Santos, A. Fernandez-Barbero, T. T. Nguyen and A. Fernandez-Nieves, *Swelling Thermodynamics of Microgel Particles*, John Wiley & Sons, Ltd, 2011, ch. 4, pp. 71–116.
- 2 B. H. Tan and K. C. Tam, *Adv. Colloid Interface Sci.*, 2008, **136**, 25–44.
- 3 V. Nigro, R. Angelini, M. Bertoldo, V. Castelvetro, G. Ruocco and B. Ruzicka, *J. Non-Cryst. Solids*, 2015, **407**, 361–366.
- 4 H.-J. Zhang, Y. Xin, Q. Yan, L.-L. Zhou, L. Peng and J.-Y. Yuan, *Macromol. Rapid Commun.*, 2012, **33**, 1952–1957.
- 5 T. T. Nguyen, *Microgel Suspensions: Fundamentals and Applications*, 2011, vol. 73.
- 6 F. Scheffold, *Nat. Commun.*, 2020, **11**, 1–13.
- 7 L. Tavagnacco, E. Zaccarelli and E. Chiessi, *Phys. Chem. Chem. Phys.*, 2018, **20**, 9997–10010.
- 8 L. Rovigatti, N. Gnan, A. Ninarello and E. Zaccarelli, *Macromolecules*, 2019, **52**, 4895–4906.
- 9 A. Scotti, M. F. Schulte, C. G. Lopez, J. J. Crassous, S. Bochenek and W. Richtering, *Chem. Rev.*, 2022, **122**, 11675–11700.
- 10 S. Meyer and W. Richtering, *Macromolecules*, 2005, **38**, 1517–1519.
- 11 N. Dingenouts, C. Norhausen and M. Ballauff, *Macromolecules*, 1998, **31**, 8912–8917.
- 12 N. Boon and P. Schurtenberger, *Phys. Chem. Chem. Phys.*, 2017, **19**, 23740–23746.
- 13 T. Kyrey, J. Witte, A. Feoktystov, V. Pipich, B. Wu, S. Pasini, A. Radulescu, M. U. Witt, M. Kruteva, R. von Klitzing, S. Wellert and O. Holderer, *Soft Matter*, 2019, **15**, 6536–6546.
- 14 M. U. Witt, S. Hinrichs, N. Möller, S. Backes, B. Fischer and R. von Klitzing, *J. Phys. Chem. B*, 2019, **123**, 2405–2413.
- 15 I. Varga, T. Gilányi, R. Mészáros, G. Filipcsei and M. Zrnyi, *J. Phys. Chem. B*, 2001, **105**, 9071–9076.
- 16 F. Schneider, A. Balaceanu, A. Feoktystov, V. Pipich, Y. Wu, J. Allgaier, W. Pyckhout-Hintzen, A. Pich and G. J. Schneider, *Langmuir*, 2014, **30**, 15317–15326.
- 17 Y. Hertle and T. Hellweg, *J. Mater. Chem. B*, 2013, **1**, 5874–5885.
- 18 R. Rivas-Barbosa, J. Ruiz-Franco, M. A. Lara-Peña, J. Cardellini, A. Licea-Claverie, F. Camerin, E. Zaccarelli and M. Laurati, *Macromolecules*, 2022, **55**, 1834–1843.
- 19 J. Vialletto, S. N. Ramakrishna, L. Isa and M. Laurati, *J. Colloid Interface Sci.*, 2024, **672**, 814–823.
- 20 A. Scotti, M. Brugnoni, C. G. Lopez, S. Bochenek, J. J. Crassous and W. Richtering, *Soft Matter*, 2020, **16**, 668–678.
- 21 J. Vialletto, S. N. Ramakrishna and L. Isa, *Sci. Adv.*, 2022, **8**, eabq2019.
- 22 S. M. Hashmi and E. R. Dufresne, *Soft Matter*, 2009, **5**, 3682–3688.



23 P. Voudouris, D. Florea, P. van der Schoot and H. M. Wyss, *Soft Matter*, 2013, **9**, 7158–7166.

24 B. Sierra-Martin, J. A. Frederick, Y. Laporte, G. Markou, J. J. Lietor-Santos and A. Fernandez-Nieves, *Colloid Polym. Sci.*, 2011, **289**, 721–728.

25 J. E. Houston, L. Fruhner, A. de la Cotte, J. R. González, A. V. Petrunin, U. Gasser, R. Schweins, J. Allgaier, W. Richtering, A. Fernandez-Nieves and A. Scotti, *Sci. Adv.*, 2022, **8**, eabn6129.

26 T. Höfken, U. Gasser, S. Schneider, A. V. Petrunin and A. Scotti, *Macromol. Rapid Commun.*, 2024, 2400043.

27 P. S. Mohanty, S. Nöjd, K. van Gruijthuijsen, J. J. Crassous, M. Obiols-Rabasa, R. Schweins, A. Stradner and P. Schurtenberger, *Sci. Rep.*, 2017, **7**, 1487.

28 G. M. Conley, P. Aebischer, S. Nöjd, P. Schurtenberger and F. Scheffold, *Sci. Adv.*, 2017, **3**, e1700969.

29 G. M. Conley, C. Zhang, P. Aebischer, J. L. Harden and F. Scheffold, *Nat. Commun.*, 2019, **10**, 2436.

30 L. Hartmann, K. Watanabe, L. L. Zheng, C.-Y. Kim, S. E. Beck, P. Huie, J. Noolandi, J. R. Cochran, C. N. Ta and C. W. Frank, *J. Biomed. Mater. Res., Part B*, 2011, **98**, 8–17.

31 M. Zhang, X. Li, Y. Gong, N. Zhao and X. Zhang, *Biomaterials*, 2002, **23**, 2641–2648.

32 K. Bjugstad, K. Lampe, D. Kern and M. Mahoney, *J. Biomed. Mater. Res., Part A*, 2010, **95**, 79–91.

33 L. Luo Zheng, V. Vanchinathan, R. Dalal, J. Noolandi, D. J. Waters, L. Hartmann, J. R. Cochran, C. W. Frank, C. Q. Yu and C. N. Ta, *J. Biomed. Mater. Res., Part A*, 2015, **103**, 3157–3165.

34 J.-F. Lutz, *J. Polym. Sci., Part A: Polym. Chem.*, 2008, **46**, 3459–3470.

35 Z. Hu, T. Cai and C. Chi, *Soft Matter*, 2010, **6**, 2115–2123.

36 J. Ruiz-Franco, R. Rivas-Barbosa, M. A. Lara-Peña, J. R. Villanueva-Valencia, A. Licea-Claverie, E. Zaccarelli and M. Laurati, *Soft Matter*, 2023, **19**, 3614–3628.

37 A. Scotti, U. Gasser, E. S. Herman, M. Pelaez-Fernandez, J. Han, A. Menzel, L. A. Lyon and A. Fernández-Nieves, *Proc. Natl. Acad. Sci. U. S. A.*, 2016, **113**, 5576–5581.

38 A. Serrano-Medina, J. Cornejo-Bravo and A. Licea-Claverie, *J. Colloid Interface Sci.*, 2012, **369**, 82–90.

39 X. Di, X. Peng and G. B. McKenna, *J. Chem. Phys.*, 2014, **140**, 054903.

40 M. Lara-Peña, A. Licea-Claverie, I. Zapata-González and M. Laurati, *J. Colloid Interface Sci.*, 2021, **587**, 437–445.

41 K. Wood, J. P. Mata, C. J. Garvey, C.-M. Wu, W. A. Hamilton, P. Abbeywick, D. Bartlett, F. Bartsch, P. Baxter, N. Booth, W. Brown, J. Christoforidis, D. Clowes, T. d'Adam, F. Darmann, M. Deura, S. Harrison, N. Hauser, G. Horton, D. Federici, F. Franceschini, P. Hanson, E. Imamovic, P. Imperia, M. Jones, S. Kennedy, S. Kim, T. Lam, W. T. Lee, M. Lesha, D. Mannicke, T. Noakes, S. R. Olsen, J. C. Osborn, D. Penny, M. Perry, S. A. Pullen, R. A. Robinson, J. C. Schulz, N. Xiong and E. P. Gilbert, *J. Appl. Crystallogr.*, 2018, **51**, 294–314.

42 S. R. Kline, *J. Appl. Crystallogr.*, 2006, **39**, 895–900.

43 J. S. Higgins and H. C. Benoît, *Polymers and Neutron Scattering*, Clarendon Press, 1st edn, 1997.

44 W. D. Dozier, J. S. Huang and L. J. Fetters, *Macromolecules*, 1991, **24**, 2810–2814.

45 J. Clara-Rahola, A. Fernandez-Nieves, B. Sierra-Martin, A. B. South, L. A. Lyon, J. Kohlbrecher and A. Fernandez Barbero, *J. Chem. Phys.*, 2012, **136**, 214903.

46 M. Shibayama, *Macromol. Chem. Phys.*, 1998, **199**, 1–30.

47 A. Scotti, U. Gasser, A. V. Petrunin, L. Fruhner, W. Richtering and J. E. Houston, *Soft Matter*, 2022, **18**, 5750–5758.

48 B. Zhou, U. Gasser and A. Fernandez-Nieves, *Nat. Commun.*, 2023, **14**, 3827.

49 M. Laurati, S. U. Egelhaaf and G. Petekidis, *J. Rheol.*, 2011, **55**, 673–706.

50 N. Koumakis, A. Pamvouoglou, A. S. Poulos and G. Petekidis, *Soft Matter*, 2012, **8**, 4271–4284.

51 K. van der Vaart, Y. Rahmani, R. Zargar, Z. Hu, D. Bonn and P. Schall, *J. Rheol.*, 2013, **57**, 1195–1209.

52 A. Ghosh, G. Chaudhary, J. G. Kang, P. V. Braun, R. H. Ewoldt and K. S. Schweizer, *Soft Matter*, 2019, **15**, 1038–1052.

53 J. C. Fernández-Toledano, J. Rodríguez-López, K. Shahrivar, R. Hidalgo-Álvarez, L. Elvira, F. Montero de Espinosa and J. de Vicente, *J. Rheol.*, 2014, **58**, 1507–1534.

54 K. N. Pham, G. Petekidis, D. Vlassopoulos, S. U. Egelhaaf, W. C. K. Poon and P. N. Pusey, *J. Rheol.*, 2008, **52**, 649–676.

55 R. G. Joshi and B. V. R. Tata, *Colloid Polym. Sci.*, 2017, **295**, 1671–1683.

56 C. Pellet and M. Cloitre, *Soft Matter*, 2016, **12**, 3710–3720.